RESEARCH ARTICLE

Types of Vertical Structure of the Nocturnal Boundary Layer

L. Mahrt[1] · **O. Acevedo[2]**

Abstract

The vertical structure of the observed stable boundary layer often deviates substantially from textbook profiles. Even over flat homogeneous surfaces, the turbulence may not be completely related to the surface conditions and instead generated by elevated sources of turbulence such as low-level jets and transient modes. In stable conditions, even modest surface heterogeneity can alter the vertical structure of the stable boundary layer. With clear skies and low wind speeds, cold-air drainage is sometimes generated by very weak slopes and induces a variety of different vertical structures. Our study examines the vertical structure of the boundary layer at three contrasting tower sites. We emphasize low wind speeds with strong stratification. At a given site, the vertical structure may be sensitive to the surface wind direction. Classification of vertical structures is posed primarily in terms of the profile of the heat flux. The nocturnal boundary layer assumes a variety of vertical structures, which can often be roughly viewed as layering of the heat-flux divergence (convergence). The correlation coefficient between the temperature and vertical velocity fluctuations provides valuable additional information for classification of the vertical structure.

Keywords Cold-air drainage · Nocturnal boundary layer · Stratified turbulence · Stable boundary layer · Vertical structure

1 Introduction

Professor Zilitinkevich organized the study of the stable boundary layer in terms of non-dimensional parameters including the gradient and flux Richardson numbers, and the Prandtl number, using a variety of sets of budget equations at different levels of complexity. This approach was generalized through incorporation of the total turbulence energy that includes fluctuations of potential energy (Zilitinkevich et al. 2007). Scaling variables were chosen to describe profiles across the boundary layer (Zilitinkevich and Esau 2007). Zilitinkevich et al. (2009) modified the similarity theory to include the impact of internal gravity waves. These studies culminated in Zilitinkevich et al. (2013) where different levels of complexity are systematically considered. Kleeorin et al. (2021) extended the analysis to transport of passive

✉ L. Mahrt
  mahrt@nwra.com

1   NorthWest Research Associates, 2171 NW Kari Pl, Corvallis, OR 97330, USA

2   Universidade Federal de Santa Maria, Santa Maria, RS 97105-900, Brazil

scalars. These studies, and citations therein, established the basic framework for the dynamics of the stable boundary layer and its vertical structure. Many subsequent observational studies were launched by different investigators to explore complications in geophysical stable boundary layers, such as surface heterogeneity, topography, generation of turbulence by low-level jets, wind-directional shear, and non-stationarity.

Our study concentrates on complexities of the vertical structure of the atmospheric boundary layer posed mainly in terms of the heat-flux profile. In simple boundary layers, the downward heat flux decreases monotonically with height, as examined by Grant (1997); see also citations within. Deviations from monotonic decrease of the downward heat flux with height may be a consequence of a variety of causes, such as turbulence generation aloft and topography. Even over homogenous surfaces, deeper "top-down" or "upside-down" boundary layers may develop where the turbulence and downward heat flux increase with height above the surface. Such turbulence can be generated by shear on the underside of the low-level jet (Banta et al. 2002; Lundquist and Mirocha 2008; Sun et al. 2012; Williams et al. 2013; Stefanello et al. 2020), shear instability induced by two-dimensional stratified "turbulence" (Högström et al. 1999), and gravity-wave breaking (Forrer and Rotach 1998; Strang and Fernando 2001; Sun et al. 2015). This top-down scenario is often associated with intermittent downward bursts of turbulence toward the surface (Nappo 1991; Roy et al. 2021), corresponding to heat-flux convergence. The magnitude of the fluxes can be a minimum at the jet-wind maximum where shear generation is weak, as observed by Conangla and Cuxart (2006) and Cuxart (2008). The heat-flux convergence below the wind maximum leads to warming unless balanced by cold-air advection, in which case the heat-flux convergence is related to non-local processes. Heat-flux convergence might be temporarily part of a non-stationary mode and may occur over a relatively deep layer (Forrer and Rotach 1998).

Downward turbulence bursting associated with low-level jets often induces significant variability of the flow near the surface (Cava et al. 2019b) and may trigger changes between boundary-layer regimes (Yus-Díez et al. 2019). Even if the mean vertical structure is not top-down, and on average the turbulence decreases with height, top-down processes may still be operating as a secondary contribution. On the other hand, Mahrt et al. (2013) found that profiles of the vertical velocity fluctuations overestimate the top-down process in the stable boundary layer because the fluctuations become increasingly non-turbulent with increasing height.

Other complex vertical structures occur over topography. Even very gentle uniform slopes, significantly less than 1%, sometimes induce drainage flows (Caughey et al. 1979). Pardyjak et al. (2009) found that the onset of drainage flows can be abrupt with multiple drainage flows from different slopes arriving at different times. Internal gravity waves are sometimes observed above the wind maximum (Viana et al. 2010). Drainage flows often generate turbulence both below and above the wind maximum. In some cases, the downward heat flux is a minimum at the wind maximum (Grachev et al. 2016), corresponding to vertical heat-flux convergence above the wind maximum. We view this layer of heat flux convergence as a transition layer. The downward heat flux reaches a maximum at the top of the transition layer and then decreases with height in an overlying regional boundary layer.

Cuxart et al. (2007) examined horizontal convergence of katabatic flows into a valley cold pool, which then descended down the valley, and subsequently over the sea as a land breeze. Mortarini et al. (2018) detailed the potential complexity of nocturnal boundary layers in terms of the interaction between the turbulence, multiple circulations driven by surface heterogeneity, and low-level jets where the downward heat flux often reaches a maximum at some level above the surface with heat convergence below this maximum. These complex scenarios are common but not well understood.

Complex vertical structure is also associated with flow over variable surface roughness and variable surface temperature, possibly leading to internal boundary layers (Garratt 1990; Bou-Zeid et al. 2020). Internal boundary layers induce a variety of different vertical structures that depend on the exact position downwind from the surface discontinuity. Even weak surface heterogeneity becomes important with low wind speeds and significant stratification. An internal boundary layer in flow over a decrease of surface roughness or decrease of surface temperature might induce weak near-surface turbulence. This surface-based layer evolves downwind into an "equilibrium layer", which has adjusted to the new surface. We expect an overlying transition layer to extend to the top of the new internal boundary layer. Above the transition layer a regional boundary layer, that is influenced by the upwind rougher surface, flows over the new internal boundary layer. Stoll and Porté-Agel (2008) show that flow from a cold surface to a warmer surface leads to heat-flux convergence near the surface (their Fig. 4) and increasing temperature in the downwind direction, while flow from a warmer surface to a cold surface can lead to heat-flux divergence and decreasing temperature in the downwind direction. Grachev et al. (2018) analyzed flux data from multiple levels on multiple towers to study the impact of surface heterogeneity of the coastal zone on the turbulence relationships and their vertical structure. Some of the observations could be framed in terms of stable or unstable internal boundary layers and the variation of the flux footprint with measurement height. Grachev et al. (2021) showed time series of fluxes of the heat flux at four levels in an irregular coastal zone that revealed complex vertical structure of the heat flux that sometimes underwent major transitions during the night.

Theoretically, the bottom of the regional boundary layer could be related to the blending height above which horizontal variations of the fluxes occur only on large horizontal scales. In practice, assessment of horizontal variation of fluxes at various levels are difficult in the stable boundary layer because aircraft are unable to fly close to the surface except for a brief period in the early morning. Decreasing horizontal variability might be inferred from the vertical structure of time variability at a fixed point, as in Fig. 12 of Medeiros and Fitzjarrald (2014). From a more general point of view, any height dependence of the horizontal pressure gradient or advection of temperature can distort the vertical structure of the boundary layer. For example, Medeiros et al. (2021) examined a multi-layer regime where the surface boundary layer is a thin nocturnal boundary layer sometimes identified as a land breeze with an overlying layer of marine air remaining from the previous day's sea breeze, capped by larger scale flow (their Fig. 14).

Our study focuses on common non-traditional vertical structures of the nocturnal boundary layer. We do not explicitly consider changes of vertical structure and character of the turbulence due to frequent non-stationary submeso modes (Sun et al. 2004; Kang et al. 2015; Mortarini et al. 2016; Vercauteren et al. 2019; Cava et al. 2019a; Boyko and Vercauteren 2021). Such motions are often important and can lead to transitions between weak turbulence and more significant turbulence and can modulate even the sign of the heat-flux divergence on a variety of time scales, as shown for example in Fig. 7 of Arrillaga et al. (2019). Non-stationarity can also strongly modify the thickness of surface-based boundary layers (Acevedo et al. 2019).

We investigate different vertical structures of the nocturnal boundary layer primarily in terms of the heat flux. The profile of the momentum flux is often more complex and is not considered herein. Although the momentum and heat flux profiles are not independent, incorporating the structure of the momentum flux is sometimes a complex study in itself that requires extensive evaluation. Our analysis will emphasize the structure of the heat flux in terms of subclasses based on wind speed, stratification, and sometimes wind direction. A
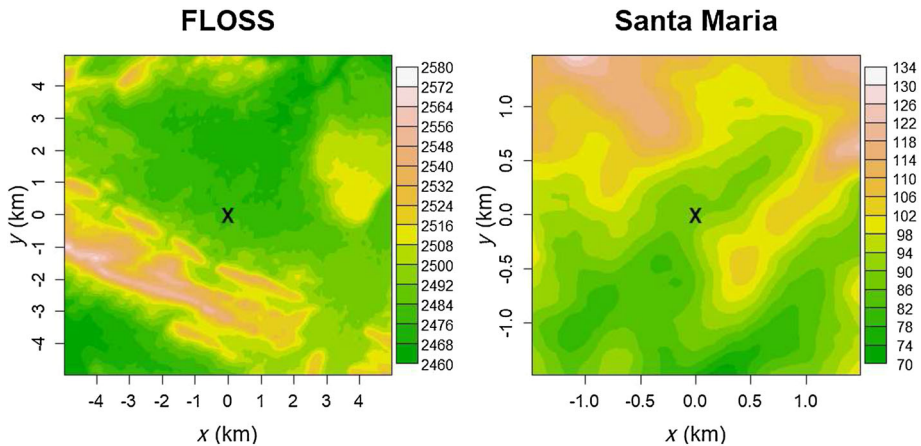
FLOSS

Santa Maria

Fig. 1 The towers for the FLOSSII site and the Santa Maria site are located with an "X". The FLOSSII map uses a larger horizontal and vertical scale to accommodate the larger-scale topography at the FLOSSII site

given subclass of vertical structure does not imply unique physics, but is useful for organizing the analysis of the measurements. In the next section, we introduce the three tower datasets.

2 Sites

We now summarize the basic characteristics of the tower sites. Sonic anemometer measurements were collected in the North Park Basin, Colorado, USA, during winter 2002–2003 in the Fluxes Over a Snow Surface II field program (FLOSSII, http://www.eol.ucar.edu/isf/projects/FLOSSII/). The FLOSSII site is modestly heterogeneous and includes grass close to the tower and scattered brush a few hundred metres upwind, depending on the wind direction. The distribution of the brush is somewhat disorganized with a typical height on the order of 0.1 m. Mahrt and Vickers (2005) provides a map of the spatial distribution of the brush and additional description of the site. Slopes are locally weak but become more significant beginning a few kilometres from the site (Fig. 1). The FLOSSII dataset includes seven levels of sonic anemometers (CSAT3, Campbell Scientific, Logan, Utah, USA) turbulence measurements on a 30-m tower and is the longest dataset of the three sites (4 months).

Guerra et al. (2018) and Stefanello et al. (2020) have analyzed measurements from the Santa Maria tower. The data analyzed were taken in the spring of 2021 using sonic anemometers deployed at 12 levels: 1.5, 3, 5, 7, 9, 11, 14, 17, 20, 23, 26, and 30 m. Fifteen levels of temperature measurements are interspersed at 0.5, 1, 2.25, 3, 4, 6, 8, 10, 12, 15.5, 18.5, 21.5, 24.5, 28, and 29.5 m. The tower was installed in an area near the University of Santa Maria, generally used for research on cattle grazing. The grass is typically 30–50 cm high. A uniform fetch of a few kilometers exists to the south-east of the tower. A suburban area begins about 500 m to the north of the tower with moderate hills of about 500 m height beginning about 5 km north of the tower. The topography at the Santa Maria site (Fig. 1) is less coherent compared to that at the FLOSSII site and is perhaps more typical of surface landscapes around the world. The tower is in a poorly defined valley characterized by a south-west–north-east axis. The most common wind direction at this site is from the south-east. Such airflow appears to be generated by cold-air drainage due to a range of low hills to the south-east of the tower. South-easterly winds are also typical of postfrontal conditions.

Table 1 Field program, surface type, duration (weeks), tower height (H (m)), height of primary wind observation (z), heights of two temperature observations for calculation of the near-surface stratification, averaging time τ (min), and a citation with more information on the site

Site	Surface	Weeks	H	z	$z1, z2$	τ	Citation
SCP	Grass*	8	20	1	0.5, 2	1	Mahrt et al. (2014)
FLOSSII	Grass*	17	30	1	1, 5	1	Mahrt (2010)
Santa Maria	grass	8	30	1.5	1, 4	1	Stefanello et al. (2020)

Grass* implies some short brush in the area with a height of generally 0.2 m or less

The Shallow Cold Pool (SCP) Experiment was conducted over semi-arid grasslands in north-east Colorado, USA, from 1 October to 1 December 2012 (https://www.eol.ucar.edu/field_projects/scp). The main valley is roughly 12 m deep and 270 m across. See Mahrt et al. (2014) and Pfister et al. (2021) for maps and additional descriptions of the site. The width of the valley floor averages about 5 m with an average down-valley slope of about 2%, increasing to about 3% at the upper end of the valley. The side slopes of the valley are on the order of 10% or less. We analyze the 1-m sonic anemometer (CSAT3, Campbell Scientific, Logan Utah, USA) observations from 19 stations and from 8 levels on the main 20-m tower. The near-surface stratification is estimated from the National Center for Atmospheric Research hygrothermometers deployed at the 0.5- and 2-m levels at 19 of the stations. The analysis in our study includes only 20-m wind directions between 290° and 360°, which is the prevailing wind direction. Additional details of the sites are listed in Table 1.

2.1 Partitioning

The flow is decomposed as

$$\phi = \phi' + \overline{\phi}, \tag{1}$$

where ϕ is potential temperature or one of the velocity components, and $\overline{\phi}$ is the average over time interval τ; ϕ' is the deviation from a local time average and is ideally dominated by turbulent fluctuations. The averaging time τ for each field program is 1 min. As an example, the kinematic heat flux is written as $\overline{w'\theta'}$.

The height dependence of the estimated heat flux can be contaminated by the omission of larger scale flux lost by the 1-min averages at higher levels. We examined the multiresolution cospectra of the heat flux as a function of height at the Santa Maria site, which includes the largest number of flux levels amongst the three sites. On average, the flux loss near the top of the tower created a 10% artificial decrease of the flux across the tower layer. This small artificial height dependence of the flux does not justify the complications associated with applying and interpreting a height-dependent averaging time. Unfortunately, the optimum averaging period also varies with time at a fixed level.

The wind speed is calculated as

$$U \equiv \sqrt{\overline{u}^2 + \overline{v}^2}. \tag{2}$$

The data are partitioned into subclasses based on wind speed, stratification, and sometimes wind direction. Compositing over classes of measurements is indicated with square brackets, for example $[\overline{w'\theta'}]$. The individual vertical structures within a given class can vary substantially between profiles. In this sense, compositing hides significant physics. A future study of
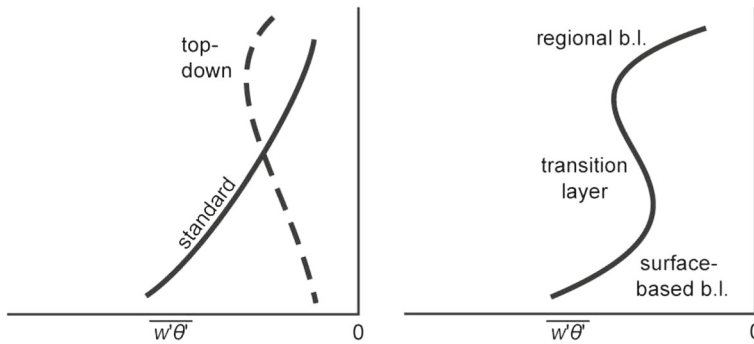
Fig. 2 Idealized vertical structures of the downward heat flux. Standard and top-down vertical structures are on the left. The right panel depicts the three-layer structure where the surface-based boundary layer includes, for example, cold-air drainage, a cold pool, or an equilibrium layer following a rough-to-smooth roughness transition

individual events will emphasize the Santa Maria site which provides high vertical resolution of the flux profiles and is still collecting data.

2.2 Idealized Layering

We now briefly summarize vertical structure based on the literature (See Introduction) that will serve as a working hypothesis for our analyses. Actual vertical structures are often more complex. The traditional nocturnal boundary layer is characterized by monotonically decreasing downward heat flux with height which becomes small at the boundary-layer top (Fig. 2, left, solid). With the top-down structure, the primary generation of the turbulence is elevated sometimes associated with shear on the underside of a low-level jet. Intermediate examples occur where both elevated and surface-based sources of turbulence are simultaneously important.

The three-layer structure (Fig. 2, right) is more complex in that a surface-based boundary layer and generation of turbulence at higher levels each dominate at their respective levels with a transition layer between. The three-layer structure results from a variety of different physical mechanisms, but the layers are generally coupled. The surface boundary layer might be associated, for example, with cold-air drainage or a cold pool, transient modes, or adjustment of the flow to changes of surface conditions. Observed internal boundary layers are difficult to categorize from tower observations because the vertical profiles evolve rapidly downwind from the surface discontinuity. The drainage flow is most likely to survive if the regional turbulence is sufficiently weak and the size of the main eddies remains smaller than the height of the wind maximum of the drainage flow. The lower part of the surface boundary layer may include a thin "surface layer" where surface similarity theory applies. This vertical structure does not have a universal physical interpretation. For example, the three-layer structure of the heat-flux profile observed in Pfister et al. (2019) (their Fig. 10, red line) occurred with more significant winds.

The heat-flux convergence in the transition layer can be balanced by cold-air advection, or it may lead to at least temporary warming. The overlying regional boundary layer responds to a larger horizontal scale. The concept of a surface-based boundary layer that responds to the local surface, and the concept of a regional boundary layer that interacts with the surface on

a larger scale, assume that the surface variation can be approximated by two main horizontal scales.

These idealized layers do not exhaust the different possibilities. Because the towers often capture only a fraction of the boundary layer, the regional boundary layer or even the transition layer may not be captured. Layering revealed by the composited profiles below is somewhat smoothed because the layer boundaries can vary significantly between individual observed samples. The layering provides a framework for organizing deviations from traditional thinking, but does not provide a rigorous theory for the vertical structure.

2.3 Classification

Because the three sites are quite different and the instrumental deployments are different, the analyses are tailored to each site, although certain analyses are common to all three sites. We partition the observations into very stable boundary layers and weakly stable boundary layers, using the wind speed at 1 m and the stratification near the surface. In addition, we include a class with weak stratification and low wind speeds, typically occurring with cloudy conditions. A more complete classification that includes downwelling radiation and variability of downwelling radiation can be found in Pfister et al. (2019). We could use the bulk Richardson number as a single parameter for classification, but the individual roles of the stratification and wind speed are not fully captured by the value of the bulk Richardson number (Fig. 5, Mahrt 2017). Because of the complexity of comparing results between sites, we adopt a simpler approach.

The stratification is defined in terms of the difference of potential temperature between two levels, $\delta_z \theta$. For the FLOSSII measurements, we define very stable cases to be U (1 m) < 2 m s $^{-1}$ and $\delta_z \theta > 1$ K, where $\delta_z \theta$ is computed between the 1-m and 5-m levels. We define weakly stable boundary layers to be U (1 m) > 2 m s $^{-1}$ and $\delta_z \theta < 1$ K. We define a third regime of weak stratification and low wind speeds as $\delta_z \theta < 0.25$ K and U (1 m) < 2 m s $^{-1}$. Basing the subclasses on the joint distribution of points (Fig. 3) is more flexible than partitioning the flow in terms of the single parameter such as the bulk Richardson number. The three classes defined in Fig. 3 are somewhat subjective but correspond to substantial differences in vertical structure.

The Santa Maria site is characterized by lower wind speeds and smaller stratification, and generally more soil moisture, humidity and cloud cover. In addition, the instrumentation levels are different compared to FLOSSII. Therefore, universal partitioning of the distribution of points in $U-\delta_z \theta$ space is not possible. For the Santa Maria site (Sect. 4, Fig. 6), the threshold wind speed U (1.5 m) that separates the weakly stable and very stable regimes is chosen to be 1.5 m s $^{-1}$ and the threshold value of $\delta_z \theta$ is chosen to be 0.5 K. For the low-wind small-stratification regime $\delta_z \theta < 0.25$ K and U (1.5 m) < 1.5 m s $^{-1}$.

We follow a different approach to analyze the SCP measurements because the shallow valley induces significant spatial variation of the local surface wind and temperature fields. The fluxes on the tower may have surface footprints that span some of the surface variability. We use $U(20$ m) at the top of the tower for the representative wind, which is above the cold pool within the valley. We use the spatial average of $\delta_z \theta$ computed from the 0.5 and 2 m temperatures at the 19 stations. The near-surface stratification estimated from the tower would is often strongly influenced by the local vertical structure of the cold pool. The very stable case is defined as $U(20) < 3$ m s $^{-1}$ and $\langle \delta_z \theta \rangle > 1.5$ K where the angle brackets define spatial averaging over the 19 stations. The weakly stable boundary layer is defined as $U(20)$
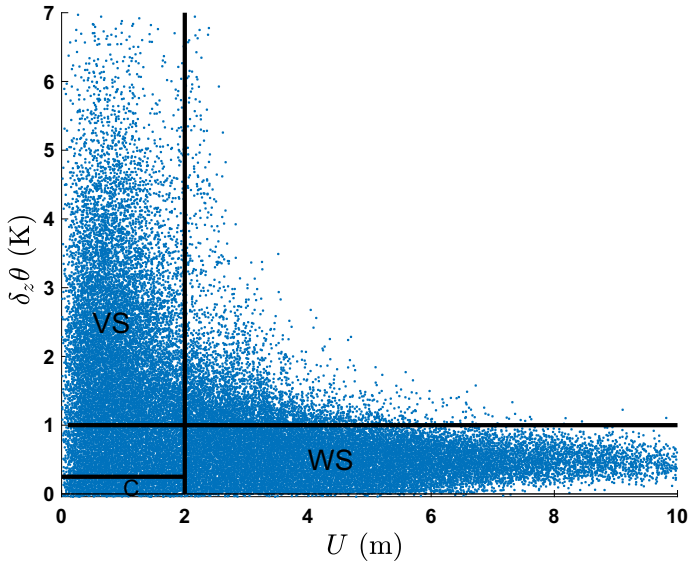
Fig. 3 The distribution of data points in $\delta_z\theta$—U (1 m) space for FLOSSII. VS casually identifies very stable conditions, WS identifies weakly stable conditions, and C identifies low wind speed and small stratification (generally cloudy conditions). The remaining unlabelled sections of data are not included in the analysis

> the 3 m s $^{-1}$ and $\delta_z\theta < 0.5$ K. The gap in the thresholds values for $\delta_z\theta$ leads to cleaner vertical profiles of the heat flux.

We impose no conditions on the heat flux. Most cases of positive heat flux are eliminated by the condition on minimum $\delta_z\theta$. Eliminating all cases with upward heat flux can convert random error to systematic error because random variations that cause upward heat flux are eliminated, but random variations that cause greater downward heat flux are retained. We also do not impose conditions on the radiation although cases of net radiative warming at the surface are largely removed by the conditions on the stratification. The standard error bars are often small because of the large sample size. However, the standard error probably seriously underestimates the error because the samples are not independent due to the non-stationarity and the small 1-min averaging window. We show error bars only when they are large enough to be easily visualized, which in the analyses below is possible for those plots where the very stable class is divided into wind-direction sectors.

3 FLOSSII Vertical Structure

3.1 Classes of Vertical Structure

We now examine the vertical structure of the profiles of the potential temperature, the scaled heat flux, and the correlation between the fluctuations of the vertical velocity and potential temperature ($R_{w\theta}$) for the three classes at the FLOSSII site. For the windy weakly stable case (black, Fig. 4b), the heat flux, scaled by the magnitude of the surface value, decreases systematically with height, as is typical of weakly stable boundary layers, and represents traditional boundary-layer structure. Upward linear extrapolation of the heat-flux profile to
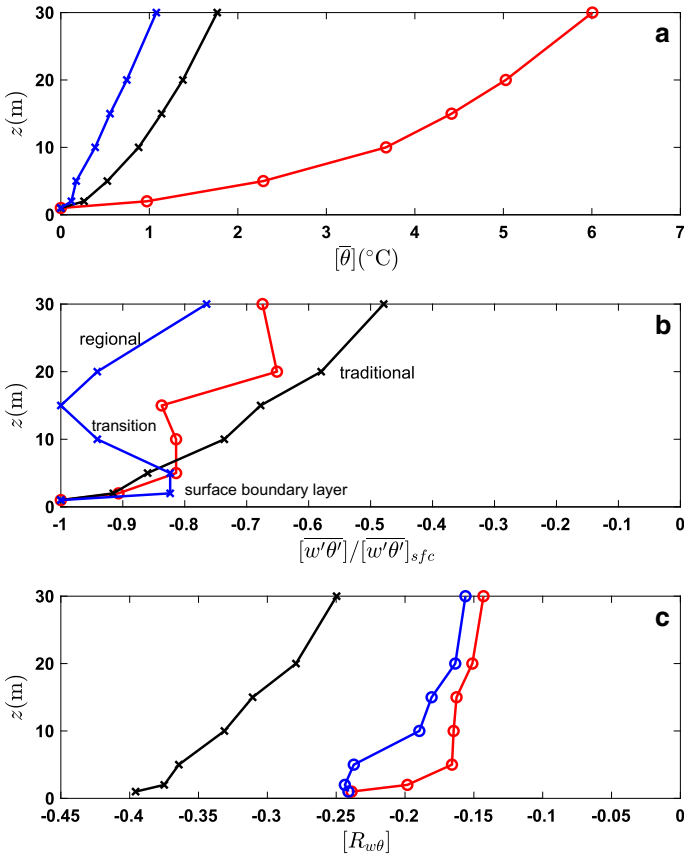
Fig. 4 FLOSSII. Composited vertical profiles for very stable conditions (red), weakly stable conditions (black), and low wind speed with small stratification (blue). Subclasses are quantitatively defined in Sect. 2.3. **a** $[\theta]$ relative to the 1-m potential temperature, **b** the surface heat flux scaled by the surface value, and **c** the correlation coefficient

zero heat-flux indicates a boundary-layer depth of roughly 40–50 m. The scaled heat-flux profile for the regime of low wind speed and weak stratification (blue, Fig. 4b) decreases with height within the first few metres, suggesting a surface-based boundary layer that achieves some degree of equilibrium with the local grass surface. The scaled heat flux increases between the 5- and 15-m levels, corresponding to a transition layer. Above 15 m, the scaled heat flux again decreases with height, as part of a regional boundary layer. The cause of this three-layer structure is not clear, although it might be explained by the upwind rougher surfaces and thus a rough-to-smooth internal boundary layer (Fig 1 in Mahrt and Vickers 2005). In this case, the "regional boundary layer" reflects the surrounding rougher surfaces. The downward heat flux originating from the upwind rougher surface is not larger than the surface downward heat flux apparently because the downward heat flux has already decayed some after leaving the rougher surface.

For the very stable case (red, Fig. 4b), the scaled heat flux decreases rapidly with height in the lowest 5 m, corresponding to a surface-based boundary layer. Between 5 and 15 m, the heat flux is roughly constant with height such that the heat flux is augmented relative to the traditional decrease of the downward heat flux with height. Because the dominant wind

direction is from the south, the augmentation of the downward heat flux might be due to advection of turbulence from the upwind brush-covered surface over the new local internal boundary layer that develops over the grass surface. In addition, a smaller number of cases of northerly flow are characterized by significant wind-direction shear above 10 m, which might also increase the downward heat flux. Our analysis is organized in terms of surface wind direction in Sect. 4.1.

For individual data points, the magnitude of the correlation coefficient, $R_{w\theta}$, is bounded by unity in contrast to the heat flux which includes outliers. Thus, compositing correlation coefficients are sometimes better posed than compositing the heat flux. The correlation coefficient [$R_{w\theta}$] for all three classes (Fig. 4c) decreases with height even when the vertical structure of the heat flux is more complex. Thus, the relative contribution of the turbulence to the fluctuations decreases with height so that the contributions of the non-turbulent motions increase with height. The magnitude of the correlation coefficient [$R_{w\theta}$] for the very stable regime (red, Fig. 4c) decreases rapidly with height within a thin surface boundary layer and then decreases gradually above 5 m. The correlation coefficient for the regime of low wind speed and weak stratification (blue) is modestly larger than that for the very stable case, suggesting that the fluctuations are more turbulent in contrast to the very stable case where w' is partly due to wave-like motions. The structure of the heat flux and attendant correlation coefficient only represent part of the boundary-layer structure.

3.2 Wind-Direction Shear

For low wind speeds at the FLOSSII site, directional shear can contribute significantly to the generation of turbulence and fluxes. The wind direction for low wind speeds is characterized by a bimodal frequency distribution with northerly surface flow or more common southerly surface flow (not shown). We partition the very stable measurements (red, Fig. 4) into these two wind-direction subgroups (Fig. 5).

We composite the vertical profiles for very stable conditions for the northerly surface flow for the sector 310°–030° (Fig. 5, cyan) with 2447 one-min records, and for southerly surface flow for the sector 160°–230° (magenta) with 5103 one-min records. The peak of the surface wind-direction distribution is about 200°. This south-south-westerly flow extends to the top of the tower with very little directional shear (magenta, Fig. 5c). This profile would be consistent with a deep drainage flow originating from upward sloping terrain south of the site (Fig. 1). Based on fair weather daytime winds, the synoptic flow is typically 250°. The downward heat flux for the south-south-westerly nocturnal flow generally decreases with height (magenta, Fig. 5a) in contrast to the very stable case with no partitioning based on wind direction where the heat-flux profile is more erratic (Fig. 3b). Although the heat-flux profile for southerly flow is somewhat noisy (Fig. 5a, magenta), it approximates the traditional decrease of the downward heat flux with height.

Inspection of time series indicates that the surface flow often changes back and forth between the two wind-direction groups. Mahrt (2010) identified this behaviour with fast-moving deep waves when the surface wind is sufficiently weak to permit domination of the surface wind direction by the wave-like motions. The change of the wind direction with time is often abrupt in the form of microfronts embedded within the wave motion. Northerly surface flow tends to be associated with cold microfronts, and southerly surface flow tends to be associated with warm microfronts, but exceptions are common (Mahrt 2010).

For the subclass of very stable northerly surface flow, the wind direction changes from about 345° at 10 m to about 210° at 30 m (cyan, Fig. 5c). The heat-flux profile for the northerly
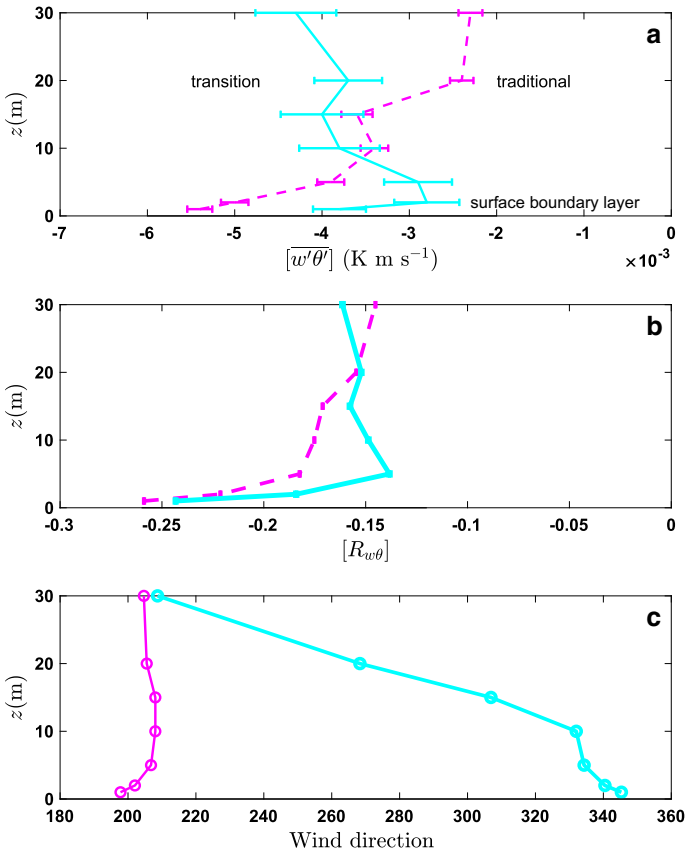
Fig. 5 FLOSSII. Composited vertical profiles for very stable conditions for the surface wind-direction groups 160°–230° (magenta) and 310°–030° (cyan)

surface flow may indicate a possible surface boundary layer in the lowest few metres (cyan). In the overlying transition layer, the downward heat flux increases with height. This increase is presumably due to the generation of turbulence by the substantial directional shear. This directional shear is computed based on the composited wind components and does not include directional shear due to deviations of the wind from the composited wind components. The downward heat flux above the wind-direction shear layer must reach a maximum above the tower and then decrease with height in an inferred regional boundary layer.

Compared to the heat flux, the vertical profile of the correlation coefficient better identifies surface boundary layers in the lowest 5 m and is less noisy (Fig. 5b). The error bars are too small to be visualized. For the northerly surface flow, the correlation coefficient increases slowly with height within the transition layer of wind-direction shear. For both wind-direction groups, the correlation coefficient decreases rapidly with height in the lowest 5 m, suggesting that the turbulent character of the fluctuations weakens rapidly with height. The rapid decrease of the correlation coefficient with height indicates that the fluctuations may become more influenced by non-turbulent motions with increasing height.
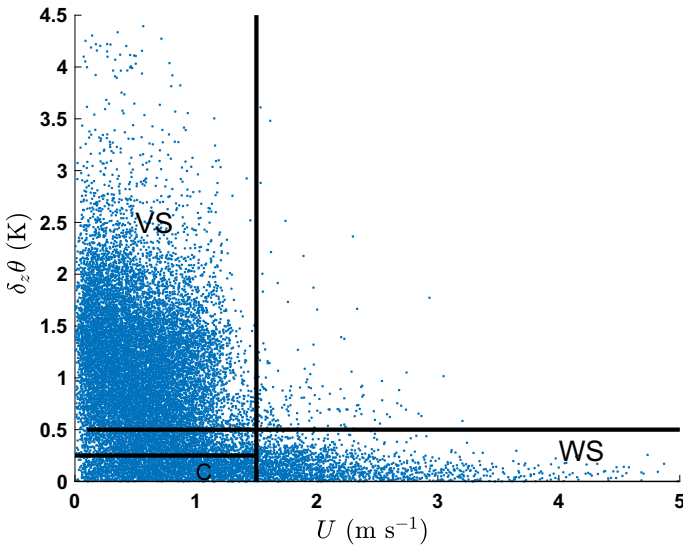
Fig. 6 The distribution of data points in $\delta_z\theta$—U (1 m) space for the Santa Maria site. VS casually identifies very stable conditions, WS identifies weakly stable conditions, and C identifies low wind speed with weak stratification (generally cloudy conditions). The remaining unlabelled sections of data are not included in the analysis

4 Santa Maria

Compared to the FLOSSII and SCP sites, the Santa Maria site is characterized by smaller $\delta_z\theta$ for a given wind speed, evidently due to greater cloud cover and greater clear-air moisture content. In addition, wind speeds at the Santa Maria site are substantially lower than at the other two sites, which leads to a relatively small number of weakly stable cases. The SCP and FLOSSII sites are dryer and at higher elevation. Figure 6 displays the distribution of the points in $\delta_z\theta - U$ space and designates the definitions of very stable, weakly stable and low wind speed with weak stratification.

The weakly stable case includes only 1150 one-min records and is not analyzed. The very stable case includes 17,260 one-min observations. The downward heat flux for the very stable case at 1.5 m (Fig. 7a, red) is 40% greater than the heat flux at 3 m (Fig. 7a), and $[R_{w\theta}]$ at the 1-m level is almost twice that at the 3-m level. The 0.5-m temperature is more than 1 K lower than the temperature at 1 m (red, right). The grass within a few metres of the tower was mowed, and the tower is in a slight depression, which may have contributed to lower temperatures very close to the surface. Thin cold-air drainage probably plays a role, discussed further below. The downward heat flux is augmented at the 1.5-m level for very stable conditions compared to higher levels, but not for the low-wind weak-stratification regime where cold-air drainage is unexpected.

At 5 m and above, the downward heat flux for the very stable case is almost independent of height. We evaluated $\delta_z\overline{w'\theta'}$, where δ_z identifies the difference between the 3-m and 26-m levels for each sample. The standard deviation of $\delta_z\overline{w'\theta'}$ is about 20 times greater than the magnitude of the composited value $[\delta_z\overline{w'\theta'}]$. Thus the composited profile of $\overline{w'\theta'}$ is a small difference between the cases of much larger heat-flux convergence and heat-flux divergence.

Eventually, the downward heat flux must decrease with height in an overlying regional boundary layer. The source of the elevated turbulence and maximum downward heat flux is
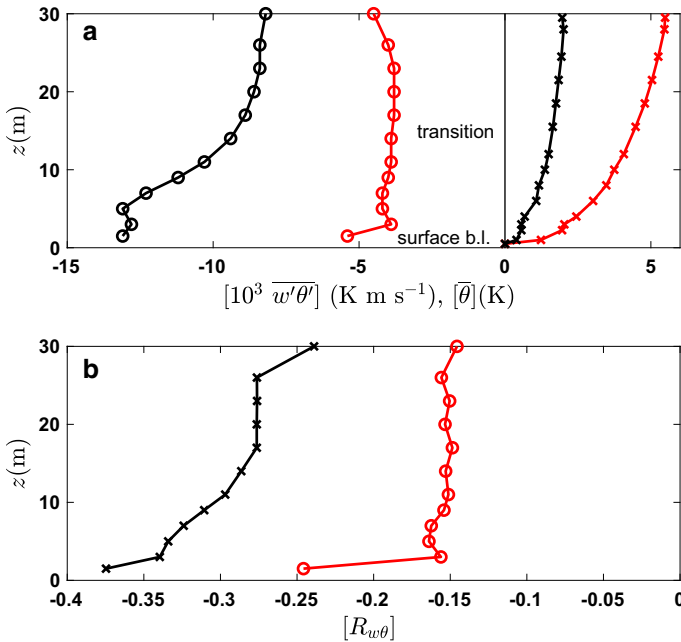
Fig. 7 The composited profiles for the Santa Maria site for the very stable class (red) and the class of low wind speeds and weak stratification (black) for **a** the heat flux (left) and $[\theta]$ relative to the 0.5-m value (right) and for **b** the correlation coefficient $R_{w\theta}$. The weakly stable boundary layer had inadequate sample size due to a lack of surface wind speeds greater than 2 m s^{-1}

not known although soundings indicated low-level jets ranging from 150 to 800 m. Section 4.1 indicates that wind-direction shear is probably an important source of turbulence generation. The correlation coefficient $[R_{w\theta}]$ at 3 m and above for the very stable case is relatively constant with height (Fig. 7b, red). The values of $[R_{w\theta}]$ are typically about 0.13 above the thin surface layer and thus comparable to those values for the very stable case at the FLOSSII and SCP sites.

As with the FLOSSII site, the heat flux is greater for the low-wind, weakly-stratified case (5849 one-min records) than the low-wind, strongly stratified case. The fluctuations in the more stratified case are probably significantly influenced by wave-like motions and other non-turbulent motions. For example, $[R_{w\theta}]$ for the subclass of greater stratification is roughly 0.13, whereas for the weak stratification, $[R_{w\theta}]$ is approximately 0.37. From another point of view, the mixing coefficients for heat, such as the eddy diffusivity, are larger with decreasing stratification although the heat flux must eventually vanish with vanishing stratification. For the low-wind weakly stratified case, the downward heat flux on the tower generally decreases with height although this decrease becomes small at the top of the tower, suggesting a much deeper boundary layer.

4.1 Wind-Direction Groups

The frequency distribution of the surface wind direction for very stable conditions (blue, Fig. 8) shows a strong peak for easterly flow and smaller peak for south-westerly flow. The winds at the top of the tower (yellow) show a peak for north-easterly flow and smaller peak for north-westerly flow. The observations for very stable conditions are therefore divided into two
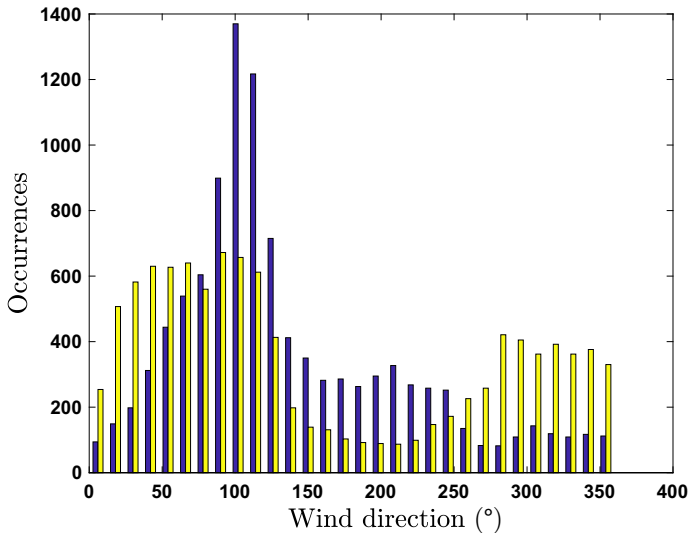
Fig. 8 Frequency distribution of the wind direction at 1.5 m (blue) and 26 m (yellow) for very stable conditions for the Santa Maria site

subclasses of surface wind direction, 60°–120° and 180°–250°. The subclass corresponding to south-westerly surface flow contains only 2266 one-min records while the subclass of easterly surface flow contains 8264 one-min records. Figure 9 indicates that both easterly surface flow (magenta) and south-westerly surface flow (cyan) rotate with height toward east-north-easterly flow near the top of the tower.

The easterly subclass of surface flow (magenta) includes cases of cold-air drainage, typically 3–5 m deep, which is currently under investigation using measurements that are still being collected. Cold-air drainage is probably responsible for the shift of the wind direction at 3 m, which aligns a little better with the local slope toward the low hills to the south-east. The large downward heat flux at the 1.5-m level and the smaller heat flux at 3 m would be consistent with increased turbulence underneath the maximum wind speed of the cold-air drainage with weaker turbulence at the wind maximum where the shear is small.

For the subclass of south-westerly surface flow (Fig. 9, cyan), the wind components for computing the wind direction at the top of the tower is vulnerable to uncertainty because the wind direction becomes quite variable at the top of the tower and the sample size for this subclass is relatively small. This point is not plotted. The apparent directional shear above the south-westerly surface flow probably leads to the observed rapid increase of downward heat flux with height (cyan), which corresponds to vertical convergence of the downward heat flux. The heat flux $\overline{w'\theta'}$ for the subclass of easterly surface flow is more independent of height compared to that for the subclass of south-westerly surface flow. The downward heat flux for both subclasses presumably begins to decrease with height above the tower in a regional boundary layer.

5 The SCP Experiment Vertical Structure

The SCP field site is significantly different from the other two sites because the local topography plays a major role, particularly in terms of sheltering and formation of cold pools on the valley floor. As a result, the analysis strategy is different.
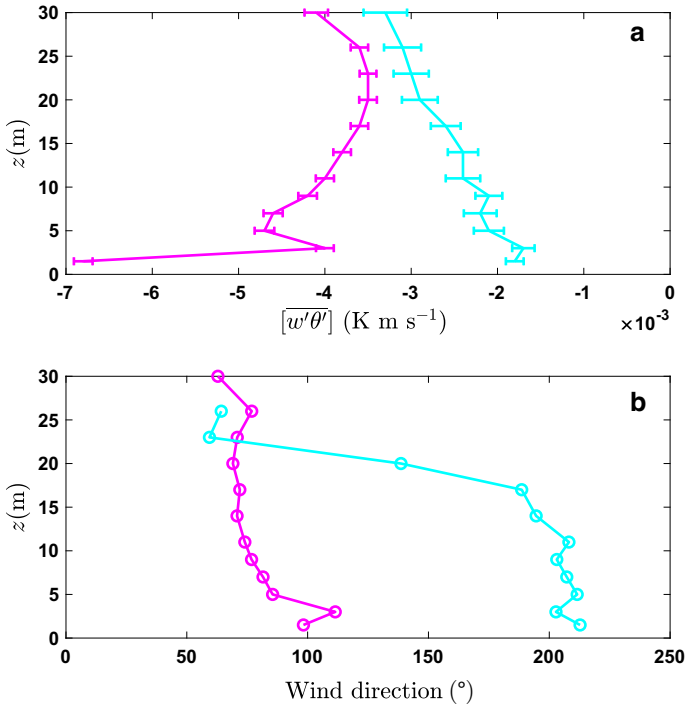
Fig. 9 The composited profiles for the Santa Maria site for the east-south-easterly surface flow (magenta) and south-westerly flow (cyan) for **a** the heat flux and **b** the wind direction

5.1 Heat-Flux Vertical Structure

For the SCP experiment, the very stable case is defined as $\langle \delta_z \theta \rangle > 1.5$ K (Sect. 2.3) and U (20 m)< 3 m s^{-1}, where the angle brackets represent a spatial average of $\delta_z \theta$ over all of the stations based on the 0.5- and 2.0-m levels. We use the average of the stratification over all of the stations instead of stratification at the base of the tower where the latter is determined by the strength of the shallow cold pool in the valley. The spatial average of the stratification over all of the 19 stations and U (20 m) are less dependent on the shallow cold pool and are statistically more robust and possibly more representative of the footprint of the fluxes on the tower above the shallow cold pool.

Figure 10 shows composited profiles of θ and $\overline{w'\theta'}$ on the tower for the very stable cases (red) and for the weakly stable cases (black); $\overline{w'\theta'}$ is scaled by the surface heat flux. In spite of the compositing, the heat-flux profile reveals distinct layers (red curve, Fig. 10a). A thin surface boundary layer corresponds to vertical divergence of the heat flux acting to cool the air in the lowest 2 m. The heat flux varies by about 20% in the lowest 2 m, implying that assumptions for surface layer similarity are not met. The depth of the surface boundary layer increases with decreasing $\langle \delta_z \theta \rangle$ and vice versa (not shown).

A transition layer from 2 to 5 m corresponds to heat-flux convergence which acts to warm the air. The heat-flux convergence might be at least partially balanced by cold-air advection. The downward heat flux reaches a local minimum at 10 m within the vertical resolution of the observations. The boundary between the transition layer and the overlying regional boundary layer is a little obscure due to the crude vertical resolution above 5 m. The regional boundary
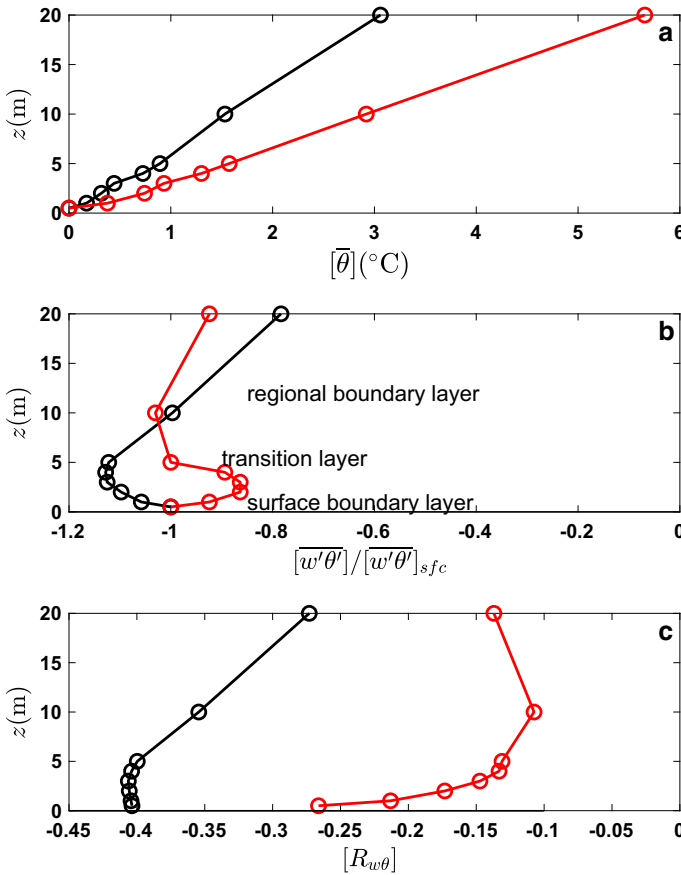
Fig. 10 SCP: Vertical structure of the composited profiles for the very stable class (red) and the weakly stable class (black) for **a** $[\theta]$ relative to the 0.5-m value, **b** the heat flux scaled by the 0.5-m value, and **c** the correlation coefficient $[R_{w\theta}]$. The definition of the classes are explained in Sect. 2.3

layer presumably interacts directly with hilltops and plateaus and perhaps the upper slopes above the cold pool although this possibility cannot be shown with certainty from the existing observations. The value of σ_w is large within the regional boundary layer (not shown), but the correlation $[R_{w\theta}]$ is small. It is not known if de-correlation occurs whenever the regional boundary layer detaches from the surface. In other terms, w' is relatively large in the regional boundary layer, but the efficiency of the transport is small (small $[R_{w\theta}]$) because σ_w is dominated by non-turbulent motions. The direction of the composited flow rotates from about 275° at the bottom of the tower at the 1-m level (wind direction roughly down-valley) to about 325° at the 20-m top of the tower, consistent with the regional slope.

For weakly stable conditions (U (20 m) > 3 m s^{-1}, $\langle \delta_z \theta \rangle$ < 0.5 K), the surface boundary layer is eliminated, but heat-flux convergence remains well defined and extends from the surface up to 5 m. The lowest 5 m could be considered as a thin top-down boundary layer. The reduced heat flux near the surface, relative to the heat flux at 5 m, might be partly due to sheltering by the valley sidewalls. The value of $[R_{w\theta}]$ (black) is roughly constant with
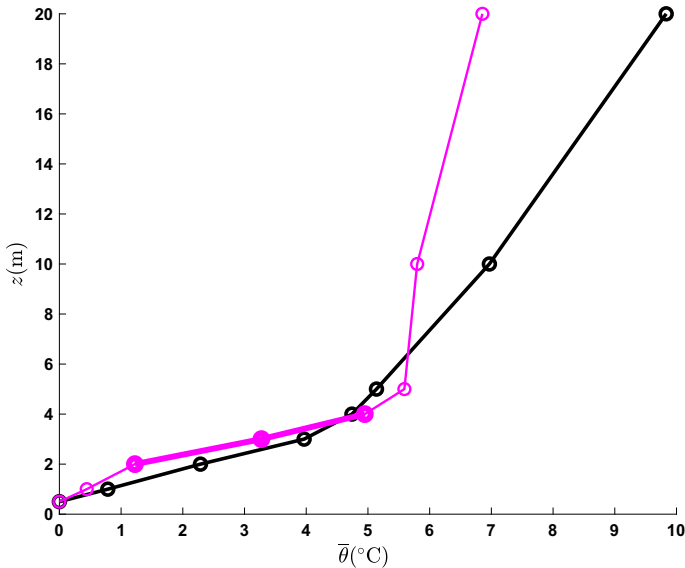
Fig. 11 Two examples of vertical structure with large stratification. The thicker part of the magenta curve identifies a possible capping inversion, which is uncommon for the cold pools at the SCP site. The black curve identifies a more typical structure with a sharp decrease of the stratification at about 3 m

height in the lowest 5 m in contrast to the very stable case where $[R_{w\theta}]$ decreases rapidly with height.

5.2 The Cold Pool "Top"

In contrast to typical schematics of cold pools, sharp capping inversions at the top of the cold pool are not common in SCP. A capping inversion requires a local maximum of stratification with weaker stratification below and above. The number of selected samples is generally small but sensitive to the algorithm for identifying a maximum stratification. An example of a strong capping inversion is the thick part of the cyan curve in Fig. 11.

The black curve in Fig. 11 shows more typical vertical structure with a significant sharp decrease of stratification with height. This rapid change of stratification with height can be included in the definition of a cold pool, that is a sharp decrease of stratification instead of a sharp increase of temperature. The vertical temperature structure sometimes varies rapidly over periods of only a few minutes (not shown), possibly indicating the influence of transient submeso motions. The sharpness of the top of the cold pool sometimes appears to be partly due to significant mixing above the cold pool.

Because the significant changes of θ or changes of stratification with height occur at a variety of different levels, such vertical changes are partially obscured in the composited profile (Fig. 10a, red). However, definition of the cold pool in terms of a surface boundary layer is well defined in terms of the composited heat-flux profile (Fig. 10b, red). In contrast, the temperature profile does not show layering and reflects the history of the heat-flux profile in a way that is not completely known. It is not completely clear if microfronts observed on the valley side slopes (Pfister et al. 2021) are sometimes part of a cold pool capping inversion that intersects with the side slope.

6 Brief Between-Site Comparisons

At the FLOSSII site for very stable conditions, a thin surface boundary layer of enhanced downward heat flux is thought to be advected from an increase of upwind roughness although adequate spatial observations were not available. However, partitioning the observations according to a bimodal distribution of the local surface wind direction suggests that a three-layer structure is defined when the surface flow is northerly underneath the prevailing (regional) southerly flow at the top of the tower. Thus, the wind-directional shear is important (Fig. 5).

The Santa Maria site for very stable conditions also has a bimodal distribution of wind direction at the surface with a prevailing wind direction at the top of the tower. The subclass with the strong directional shear corresponds to increasing downward heat flux with height (Fig. 9) that presumably reaches a maximum above the tower layer. The other subclass is more complex. The vertical structure is least understood at the Santa Maria site perhaps because the terrain is sufficient to modify the very stable flow but not strong enough to totally organize the vertical structure. Additional analysis is underway.

The prevailing regional flow for SCP is north-westerly while the down-valley flow is west-north-westerly so that the directional shear is generally weak. For very stable conditions, the valley cold pool leads to the three-layer structure where down-valley flow at the surface transitions to regional flow in the upper part of the 20-m tower (Fig. 10). Even the weakly stable case at the SCP site shows some impact of the shallow valley on the vertical structure.

7 Conclusions

As noted in the Introduction, non-traditional vertical structures of the nocturnal boundary layer sometimes occur even at sites considered to be relatively flat and homogeneous. Top-down boundary layers correspond to turbulence generated at higher levels and transported downward toward the surface. The downward heat flux may increase with height, corresponding to heat-flux convergence. The downward heat flux reaches an overlying maximum and then decreases with height in a regional boundary layer.

We found three-layer structures with a transition layer of heat-flux convergence between a local surface-based boundary layer and an overlying regional boundary layer. The transition layer may contain significant wind-directional shear. Local surface-based boundary layers include cold-air drainage, cold pools, and flow over surface heterogeneity. The correlation between the temperature and vertical velocity fluctuations is a measure of the efficiency of turbulent transport and provides additional support for interpretation of the vertical structure of the heat flux.

A fraction of the composited profiles do not fit into one of the prototype structures. Although the different non-traditional vertical structures of the heat flux are more likely to occur with weak winds and large stratification, we did not attempt to formulate a theory for the dependence of the vertical structure on stability, which is site dependent and wind-direction dependent. The above concept of the layering is based primarily on the heat flux and is not necessarily applicable to the momentum flux. The concept of layering provides a framework for organizing the discussions but does not serve as a general theory for the vertical structure.

Compositing profiles filters out considerable information on the variability of the profiles within a given subclass. Future case studies are planned. The amount of coupling between layers and associated transfer coefficients require investigation. More progress would benefit

from longer datasets such as one year or more. For example, after dividing the current data into categories based on wind speed and stratification, and subsequently partitioning into wind-direction sectors, the sample size can become marginal for establishing complex vertical structure. Future work will also examine individual events at the Santa Maria tower where flux data are still being collected with high vertical resolution.

References

Acevedo O, Maroneze R, Costa FD, Puhales FS, Degrazia GA, Martins LGN, Oliveira PES, Mortarini L (2019) The nocturnal boundary layer transition from weakly to very stable. Part I: observations. Q J R Meteorol Soc 145:3577–3592

Arrillaga JA, Yagüe G, Román-Cascón C, Sastre M, Maqueda G, Vilà-Guerau de Arellano J (2019) From weak to intense downslope winds: origin, interaction with boundary-layer turbulence and impact on CO_2 variability. Atmos Chem Phys 19:4615–4635

Banta R, Newsom R, Lundquist J, Pichugina Y, Coulter R, Mahrt L (2002) Nocturnal low-level jet characteristics over Kansas during CASES-99. Boundary-Layer Meteorol 105:221–252

Bou-Zeid E, Anderson W, Katul GG, Mahrt L (2020) The persistent challenge of surface heterogeneity in boundary-layer meteorology: a review. Boundary-Layer Meteorol 177:227–245

Boyko V, Vercauteren N (2021) Multiscale shear forcing of turbulence in the nocturnal boundary layer: a statistical analysis. Boundary-Layer Meteorol 179:43–72

Caughey S, Wyngaard J, Kaimal J (1979) Turbulence in the evolving stable boundary layer. J Atmos Sci 36:1041–1052

Cava D, Mortarini L, Anfossi D, Giostra U (2019a) Interaction of submeso motions in the Antarctic stable boundary layer. Boundary-Layer Meteorol 171:151–173

Cava D, Mortarini L, Giostra U, Acevedo O, Katul G (2019b) Submeso motions and intermittent turbulence across a nocturnal low-level jet: a self-organized criticality analogy. Boundary-Layer Meteorol 172:17–43

Conangla L, Cuxart J (2006) On the turbulence in the upper part of the low-level jet: an experimental and numerical study. Boundary-Layer Meteorol 118:379–400

Cuxart J (2008) Nocturnal basin low-level jets: an integrated study. Ann Geophys 56:100–113

Cuxart J, Jiménez M, Martínez D (2007) Nocturnal mesobeta basin and katabatic flows on a midlatitude island. Mon Weather Rev 135:918–932

Forrer J, Rotach M (1998) On the turbulence structure in the stable boundary layer over the greenland ice sheet. Boundary-Layer Meteorol 85:111–136

Garratt JR (1990) The internal boundary layer—a review. Boundary-Layer Meteorol 50:171–203

Grachev A, Leo LS, Sabatino SD, Fernando HJS, Pardyjak ER, Fairall CW (2016) Structure of turbulence in katabatic flows below and above the wind-speed maximum. Boundary-Layer Meteorol 159:469–494

Grachev A, Leo LS, Fernando HJS, Fairall CW, Creegan E, Blomquist B, Christman A, Hocut C (2018) Air-sea/land interaction in the coastal zone. Boundary-Layer Meteorol 167:181–210

Grachev A, Krishnamurthy R, Fernando HJS, Fairall CW, Bardoel L, Wang S (2021) Atmospheric turbulence measurements at a coastal zone with and without fog. Boundary-Layer Meteorol 181:395–422

Grant A (1997) An observational study of the evening transition boundary layer. Q J R Meteorol Soc 123:657–677

Guerra VS, Acevedo OC, Medeiros LE, Oliveira PES, Santos DM (2018) Small-scale horizontal variability of mean and turbulent quantities in the nocturnal boundary layer. Boundary-Layer Meteorol 169:395–411

Högström U, Smedman AS, Bergström H (1999) A case study of two-dimensional stratified turbulence. J Atmos Sci 56:959–976

Kang Y, Belušić D, Smith-Miles K (2015) Classes of structures in the stable atmospheric boundary layer. Q J R Meteorol Soc 141:2057–2069

Kleeorin N, Rogachevskii I, Zilitinkevich S (2021) Energy and flux budget closure theory for passive scalar in stably stratified turbulence. Phys Fluids. https://doi.org/10.1063/5.0052786

Lundquist J, Mirocha J (2008) Interaction of nocturnal low-level jets with urban geometries as seen in joint urban 2003 data. J Appl Meteorol Climatol 47:44–58

Mahrt L (2010) Common microfronts and other solitary events in the nocturnal boundary layer. Q J R Meteorol Soc 136:1712–1722

Mahrt L (2017) Heat flux in the strong-wind nocturnal boundary layer. Boundary-Layer Meteorol 163:161–177

Mahrt L, Vickers D (2005) Boundary-layer adjustment over small-scale changes of surface heat flux. Boundary-Layer Meteorol 116:313–330

Mahrt L, Thomas CK, Richardson S, Seaman N, Stauffer D, Zeeman M (2013) Non-stationary generation of weak turbulence for very stable and weak-wind conditions. Boundary-Layer Meteorol 177:179–199

Mahrt L, Sun J, Oncley SP, Horst TW (2014) Transient cold air drainage down a shallow valley. J Atmos Sci 71:2534–2544

Medeiros DG, Fitzjarrald D (2014) Stable boundary layer in complex terrain. Part I: linking fluxes and intermittency to an average stability index. J Appl Meteorol Climatol 53:2196–2215

Medeiros LE, Fisch G, Acevedo O, Costa FD, Iriart P, Anabor V, Schuch D (2021) Low-level atmospheric flow at the central north coast of Brazil. Boundary-Layer Meteorol 180:289–317

Mortarini L, Stefanello M, Degrazia G, Roberti D, Castelli ST, Anfossi D (2016) Characterization of wind meandering in low-wind-speed conditions. Boundary-Layer Meteorol 161:165–182

Mortarini L, Cava D, Giostra U, Acevedo O, Nogueira Martins LG, Soares de Oliveira PE, Anfossi D (2018) Observations of submeso motions and intermittent turbulent mixing across a low level jet with a 132-m tower. Q J R Meteorol Soc 144:172–183

Nappo C (1991) Sporadic breakdown of stability in the PBL over simple and complex terrain. Boundary-Layer Meteorol 54:69–87

Pardyjak E, Fernando H, Hunt CR, Grachev A, Anderson J (2009) A case study of the development of nocturnal slope flows in a wide open valley and associated air quality implications. Meteorol Z 18:085–100

Pfister L, Sayde C, Selker J, Mahrt L, Thomas CK (2019) Classifying the nocturnal boundary layer into temperature and flow regimes. Q J R Meteorol Soc 145:1515–1534

Pfister L, Lapo K, Mahrt L, Thomas CK (2021) Thermal submeso motions in the nocturnal stable boundary layer Part 1: detection and mean statistics. Boundary-Layer Meteorol 180:187–202

Roy S, Sentchev A, Schmitt FG, Augustin P, Fourmentin M (2021) Impact of the nocturnal low-level jet and orographic waves on turbulent motions and energy fluxes in the lower atmospheric boundary layer. Boundary-Layer Meteorol 180:527–542

Stefanello M, Cava D, Giostra U, Acevedo O, Degrazia G, Anfossi D, Mortarini L (2020) Influence of submeso motions on scalar oscillations and surface energy balance. Q J R Meteorol Soc 146:889–903

Stoll R, Porté-Agel F (2008) Large-eddy simulation of the stable atmospheric boundary layer using dynamic models with different averaging schemes. Boundary-Layer Meteorol 126:1–28

Strang EJ, Fernando HJS (2001) Entrainment and mixing in stratified shear flows. J Fluid Mech 428:349–386

Sun J, Lenschow DH, Burns SP, Banta RM, Newsom RK, Coulter R, Frasier S, Ince T, Nappo C, Balsley B, Jensen M, Mahrt L, Miller D, Skelly B (2004) Atmospheric disturbances that generate intermittent turbulence in nocturnal boundary layers. Boundary-Layer Meteorol 110:255–279

Sun J, Mahrt L, Banta RM, Pichugina YL (2012) Turbulence regimes and turbulence intermittency in the stable boundary layer during CASES-99. J Atmos Sci 69:338–351

Sun J, Nappo CJ, Mahrt L, Belušić D, Grisogono B, Stauffer DR, Pulido M, Staquet C, Jiang Q, Pouquet A, Yagüe C, Galperin B, Smith RB, Finnigan JJ, Mayor SD, Svensson G, Grachev AA, Neff WD (2015) Review of wave-turbulence interactions in the stable atmospheric boundary layer. Rev Geophys 53:965–993

Vercauteren N, Boyko V, Kaiser A, Belušić D (2019) Statistical investigations of flow structures in different regimes of the stable boundary layer. Boundary-Layer Meteorol 173:143–164

Viana S, Terradellas S, Yagüe C (2010) Analysis of gravity waves generated at the top of a drainage flow. J Atmos Sci 67:3949–3966

Williams A, Chambers S, Griffiths S (2013) Bulk mixing and decoupling of the stable nocturnal boundary layer characterized using a ubiquitous natural tracer. Boundary-Layer Meteorol 149:381–402

Yus-Díez J, Udina M, Soler MR, Lothon M, Nilsson E, Bech J, Sun J (2019) Nocturnal boundary layer turbulence regimes analysis during the BLLAST campaign. Atmos Chem Phys 19:9495–9514

Zilitinkevich S, Esau I (2007) Similarity theory and calculation of turbulent fluxes at the surface for stably stratified atmospheric boundary layers. Boundary-Layer Meteorol 125:193–205

Zilitinkevich S, Elperin T, Kleeorin N, Rogachevskii I (2007) Energy-and flux-budget (EFB) turbulence closure model for stably stratified flows. Part I: steady state homogeneous regimes. Boundary-Layer Meteorol 125:167–191

Zilitinkevich S, Elperin T, Kleeorin N, L'vov V, Rogachevskii I (2009) Energy- and flux-budget turbulence closure model for stably stratified flows. Part II: the role of internal gravity waves. Boundary-Layer Meteorol 133:139–164

Zilitinkevich S, Elperin T, Kleeorin N (2013) A hierarchy of energy- and flux-budget- (EFB) turbulence closure models for stably-stratified geophysical flows. Boundary-Layer Meteorol 146:341–373

Publisher's Note Springer Nature remains neutral with regard to jurisdictional claims in published maps and institutional affiliations.